Journal of Structural Geology 32 (2010) 2009–2021

Contents lists available at ScienceDirect

Journal of Structural Geology

journal homepage: www.elsevier.com/locate/jsg

Monoclinic and triclinic 3D flanking structures around elliptical cracks

Ulrike Exner [a,*], Marcin Dabrowski [b]

[a] University of Vienna, Department of Geodynamics and Sedimentology, Althanstrasse 14, 1090 Vienna, Austria
[b] Physics of Geological Processes, University of Oslo, Pb 1048 Blindern, 0316 Oslo, Norway

ARTICLE INFO

Article history:
Received 28 August 2009
Received in revised form
26 July 2010
Accepted 13 August 2010
Available online 20 August 2010

Keywords:
Fault-related folds
Monoclinic flow
Analytical model
Eshelby's solution
Sheath folds

ABSTRACT

We use the Eshelby solution modified for a viscous fluid to model the evolution of three-dimensional flanking structures in monoclinic shear zones. Shearing of an elliptical crack strongly elongated perpendicular to the flow direction produces a cylindrical flanking structure which is reproducible with 2D plane strain models. In contrast, a circular or even narrow, slit-shaped crack exhibits a reduced magnitude of the velocity jump across the crack and results in smaller offset and a narrower zone of deflection than predicted with 2D-models. Even more significant deviations are observed if the crack axes are oriented at an oblique angle to the principal flow directions, where the velocity jump is oblique to the resolved shear direction and is modified during progressive deformation. The resulting triclinic geometry represents a rare example of triclinic structures developing in monoclinic flow and may be used to estimate the flow kinematics of the shear zone.

© 2010 Elsevier Ltd. All rights reserved.

1. Introduction

A flanking structure is a set of deflections of marker surfaces adjacent to a slip surface, commonly a crack or vein (Passchier, 2001). Analytical (Kocher and Mancktelow, 2005; Grasemann et al., 2005; Mulchrone, 2007), numerical (Grasemann et al., 2003; Wiesmayr and Grasemann, 2005; Kocher and Mancktelow, 2006) and analogue studies (Exner et al., 2004) demonstrated the wide variability in flanking structure geometry. This variability depends on (1) the initial orientation of the crack relative to the set of marker surfaces; and (2) the kinematics of the bulk flow. These studies established the possibilities and limits of the application of flanking structures to determine shear sense and estimate the kinematic vorticity number and finite strain from geometrical characteristics.

Similar to other shear sense indicators, field examples of flanking structures are usually sought within two-dimensional sections oriented orthogonal to the layering and parallel to the tectonic transport direction (highlighted e.g. by a mineral lineation). For this kind of exposure, two-dimensional models of flanking structures are appropriate, assuming that the crack is strongly elongated perpendicular to the shear direction and deforms under plane strain flow conditions. However, some outcrops present a three-dimensional, monoclinic structure, where a foliation plane is deflected around a crack of limited length perpendicular to the shear direction. Notably, in such a geometric configuration the mineral lineation is not laterally displaced along the crack, but can be followed continuously across the structure along a straight line (indicated in Fig. 1a). Alternatively, cracks may also be oriented at an oblique angle to the mineral lineation. In these cases, the lineation additionally is displaced laterally along the crack and a deflection of the lineation is observed within the foliation plane (Fig. 1b–d).

Such effects around three-dimensional cracks cannot be studied with two-dimensional models, especially if movement occurs out of the observation plane. Thus, we apply an analytical solution of elliptical inclusions in viscous flow to investigate the effect of the crack's (1) aspect ratio, (2) orientation and (3) the background flow kinematics on geometry of the resulting flanking structure in three dimensions.

2. Model formulation

We model a flanking structure as the structure formed in the flow about an elliptical crack in a homogeneous isotropic viscous medium. Mechanical anisotropy or layers of different viscosity may be present in the natural structure, but they are neglected here. The contact between the crack surfaces is frictionless and a jump in the tangential component of velocity across the crack occurs at zero shear stress. In the model implementation, to achieve this, the

* Corresponding author. Fax: +43 1 4277 9534.
E-mail addresses: ulrike.exner@univie.ac.at (U. Exner), marcind@fys.uio.no (M. Dabrowski).

0191-8141/$ – see front matter © 2010 Elsevier Ltd. All rights reserved.
doi:10.1016/j.jsg.2010.08.002

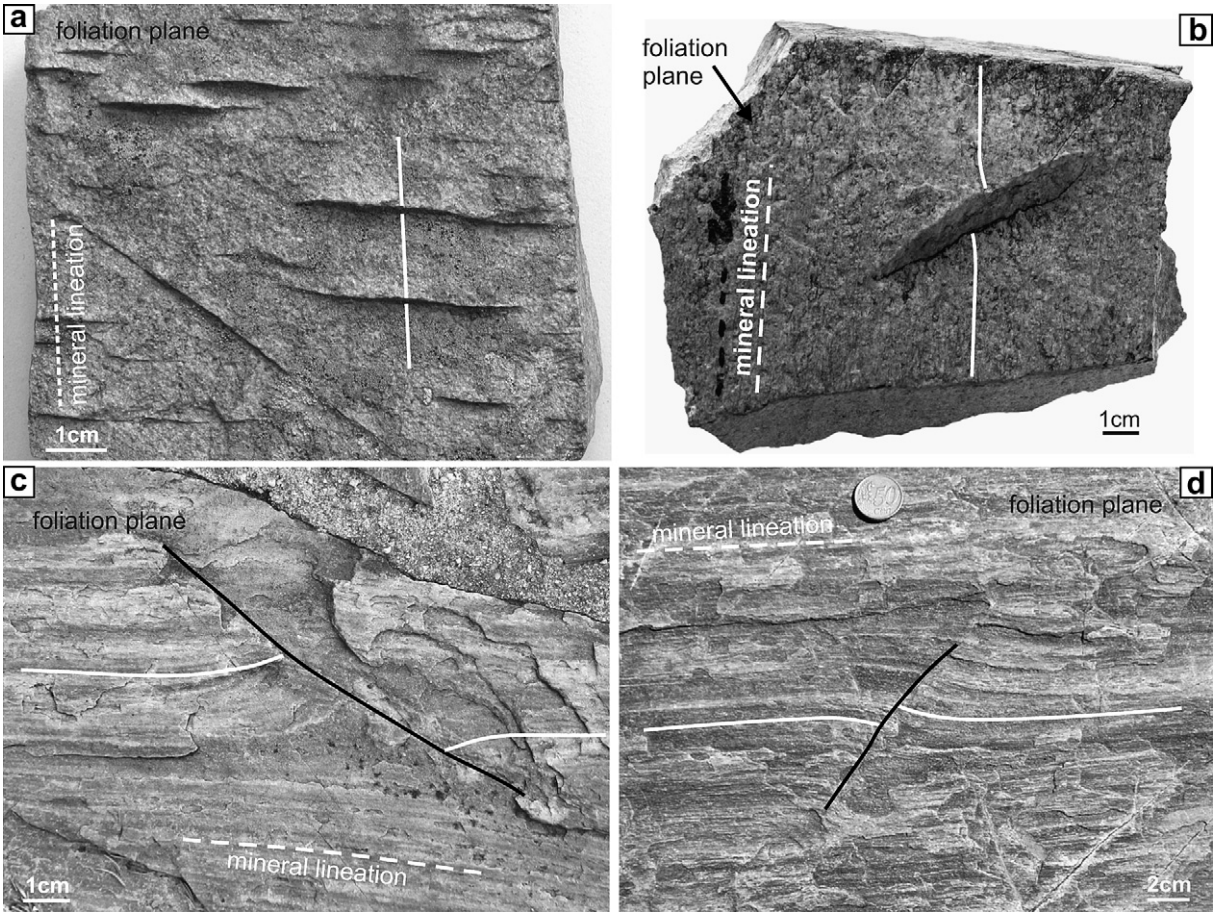

Fig. 1. Natural examples of 3D flanking structures from Antiparos (a) and Serifos (b–d), Greece, cutting across foliation planes of greenschist to amphibolites facies mylonites. (a) Several monoclinic flanking structures aligned perpendicular to the mineral lineation offset and bend the foliation, while the lineation remains straight. Triclinic flanking structures in (b–d) are oriented oblique to the mineral lineation, and deflect both the foliation and the mineral lineation.

crack is filled with an infinitesimally thin layer of incompressible inviscid fluid.

The velocity jump results in the relative displacement of pairs of particles that are initially adjacent on the two faces of the crack. Crack opening is prevented by the presence of the incompressible material filling it; a normal velocity jump is not allowed. Crack propagation does not take place, but the crack stretches and rotates during deformation of the viscous medium. Such a structure has been termed a stretching fault by Means (1989).

To obtain the pattern of surfaces deformed about this inhomogeneity during a finite deformation, we track the deformation of sets of initial marker lines and planes. Only far-field plane flow in pure shear and in simple shear is considered here. In irrotational pure shear, the far-field velocity components are

$$v_x^{(\infty)} = D_{xx}^{(\infty)} x, \quad v_y^{(\infty)} = 0, \quad v_z^{(\infty)} = -D_{xx}^{(\infty)} z \tag{1}$$

For this case, the marker planes are oriented perpendicular to the direction of maximum shortening (*xy*-planes) and the marker lines are parallel to the direction of maximum stretching (*x*-direction). In simple shear, the far-field velocity components are

$$v_x^{(\infty)} = 2D_{xz}^{(\infty)} z, \quad v_y^{(\infty)} = 0, \quad v_z^{(\infty)} = 0 \tag{2}$$

The marker planes are parallel to *xy*-planes (*shear plane*) and the marker lines are parallel to the *x*-direction (*shear direction*). In both cases, simple and pure shear, marker planes and marker lines are placed at orientations that remain unchanged under the far-field flow and as such they approximate the late-stage foliation and lineation, respectively.

3. Analysis

3.1. Reference frames

The far-field flows described in Eqs. (1) and (2) are referred to a fixed reference system *xyz* with the unit base vectors $\vec{e}_x$, $\vec{e}_y$ and $\vec{e}_z$. The crack semi-axes $\vec{a}$, $\vec{b}$ and the normal vector $\vec{c}$ determine the orientation of the unit base vectors $\vec{e}_{x'}$, $\vec{e}_{y'}$ and $\vec{e}_{z'}$ of a rotating crack reference system $x'y'z'$. The lengths of the semi-axes are *a* and *b*.

The center of the crack coincides with the common origin of these two reference systems (Fig. 2). The position of the crack center is fixed during deformation due to the symmetry. Using the three Euler angles ψ_1, φ, ψ_2 allows us to describe an arbitrary crack orientation with respect to the fixed reference frame (e.g. Goldstein et al., 2002). Imagining that the two systems are initially coincident, the *xyz* system is brought into coincidence with the crack axes by a sequence of rotations. It is firstly rotated by an angle ψ_1 around the axis $\vec{z}$; next, it is rotated around the axis $\vec{y}'$ by an angle φ. The final rotation is performed around the axis $\vec{z}'$ by an angle ψ_2. The rotation axes and their order follow the *z*–*y*–*z* convention used for Euler angles. Positive angles are measured clockwise.

For expository convenience, we speak of the *xy*-plane as horizontal. Then, ψ_1 measures the strike, or the angle between the

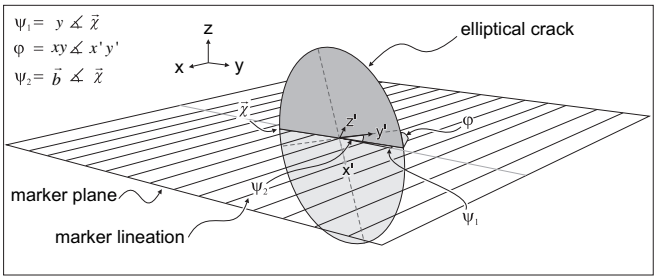

Fig. 2. Setup and model parameters: an elliptical crack with the semi-axes $\vec{a}$ and $\vec{b}$ (parallel to x' and y') is oriented at the angles ψ_1, φ and ψ_2 to the external reference frame (xyz). A passive marker plane and the lineation (in x-direction) are oriented parallel to the flow plane (xy) and shear direction (x) of the homogeneous monoclinic background flow. The line $\vec{\chi}$ marks the intersection between the crack surface ($x'y'$) and the xy-plane.

y-direction and the line of nodes $\vec{\chi}$, where the latter is the intersection of the horizontal marker plane and the plane of the crack. The dip of the crack is given by the dihedral angle φ. The angle ψ_2 measures the rotation between the semi-axis $\vec{b}$ and the line of nodes $\vec{\chi}$.

We introduce the rotation matrix **R** whose columns are the direction cosines of the crack base vectors with respect to the fixed coordinates. In terms of the Euler angles,

$$\mathbf{R} = \begin{pmatrix} \cos(\psi_1)\cos(\psi_2) - \sin(\psi_1)\cos(\varphi)\sin(\psi_2) & -\cos(\psi_1)\sin(\psi_2) - \sin(\psi_1)\cos(\varphi)\cos(\psi_2) & \sin(\varphi)\sin(\psi_1) \\ \sin(\psi_1)\cos(\psi_2) + \cos(\psi_1)\cos(\varphi)\sin(\psi_2) & -\sin(\psi_1)\sin(\psi_2) + \cos(\psi_1)\cos(\varphi)\cos(\psi_2) & -\sin(\varphi)\cos(\psi_1) \\ \sin(\psi_2)\sin(\varphi) & \cos(\psi_2)\sin(\varphi) & \cos(\varphi) \end{pmatrix} \tag{3}$$

The rotation matrix is used to transform components of vectors and tensors between the two reference frames. For instance, position vectors $\vec{r}$ are transformed according to

$$\begin{pmatrix} x' \\ y' \\ z' \end{pmatrix} = \mathbf{R}^{\mathbf{T}} \begin{pmatrix} x \\ y \\ z \end{pmatrix} \tag{4}$$

where the superscript **T** stands for the transpose.

3.2. Analytical solution

The velocity field about the elliptical crack considered here is obtained as a limiting case of a general solution for a homogeneous ellipsoidal inclusion derived by Eshelby (1957). The Eshelby solution provides the displacement field inside (Eshelby, 1957) and outside (Eshelby, 1959) an ellipsoidal homogeneous inclusion whose elastic properties differ from those of the surrounding isotropic matrix. A key characteristic of the Eshelby solution is that a uniform strain in the far-field results in a uniform strain within the inclusion. Setting the Poisson ratio to 1/2, replacing the shear modulus of each material by its viscosity and treating displacement as velocity yields the solution for the corresponding problem for a viscous inclusion in a viscous matrix (e.g. Freeman, 1987). The solution yields a constant velocity gradient $\boldsymbol{L}^{(\mathrm{incl})}$ inside the ellipsoidal inclusion for a constant velocity gradient $\mathbf{L}^{(\infty)}$ in the far field. The system of linear equations giving $\boldsymbol{L}^{(\mathrm{incl})}$ in terms of $\mathbf{L}^{(\infty)}$ is given in Appendix A.

The solution for the crack requires taking two limits: the length of inclusion axis $\vec{c}$ goes to zero and the inclusion viscosity goes to zero. The analysis shows the unbounded growth of the two components of $\boldsymbol{L}^{(\mathrm{incl})}$ (see Appendix A) that upon scaling by the infinitesimal length c determine a finite jump of the velocity across the crack (Kassir and Sih, 1975; Mura, 1987).

The velocity field in the matrix is obtained by reducing the elastic solution presented by Eshelby (1959) for the case of an incompressible matrix containing a flat ellipsoidal crack filled with an inviscid fluid. Details about the implementation of the solution and generation of 2D- and 3D-graphs are provided in Appendix B.

The crack itself is found to undergo a homogeneous deformation that results in stretching and rotation but preserves an elliptical shape. This allows us to reuse the solution to evaluate the velocity field after readjusting the shape parameters and reevaluating the components of the far-field velocity gradient in the rotating crack reference frame. We determine the evolution of a flanking structure by integrating the velocity field in the matrix.

3.2.1. Velocity field at the crack interface

The velocity field within the ellipsoidal inhomogeneity is a linear function of the position vector (see Appendix A)

$$\vec{v}^{\mathrm{incl}} = \mathbf{L}^{(\mathrm{incl})}\vec{r} \tag{5}$$

In the limit of $c \to 0$ and $\mu^{incl}/\mu^{host} \to 0$, the inclusion becomes a crack-like feature enclosed by two surfaces $z = \pm c\sqrt{1-(x'/a)^2-(y'/b)^2}$ separated with a thin film comprising an incompressible inviscid fluid. The velocity gradient tensors $\boldsymbol{L}^{(crack)}$ and $\mathbf{L}^{(\infty)}$ are equal to each other, except for components $L_{xz}^{\prime(crack)}$ and $L_{yz}^{\prime(crack)}$ that become infinite for non-vanishing $D_{xz}^{\prime(\infty)}$ and $D_{yz}^{\prime(\infty)}$. However, the products $L_{xz}^{\prime(crack)}c$ and $L_{yz}^{\prime(crack)}c$ remain bounded and the velocity field at the two interfaces is

$$\vec{v}^{\pm(crack)} = \mathbf{L}^{(\infty)}\vec{r} \pm \vec{v}^{(c)}\sqrt{1-(x'/a)^2-(y'/b)^2} \tag{6}$$

where the superscript $\pm$ differentiates between the velocity field on the top $z' \to 0^+$ and the bottom $z' \to 0^-$ interface of the crack.

The part of the velocity field given in the first term in Eq. (6) is not vanishing at the crack rim and it describes the stretching and rotation of the crack. The velocity vectors in the points lying at the crack rim are found by evaluating the homogeneous background velocity field in them. The velocity vector at the crack center $\vec{v}^{(c)}$ for $z \to 0^+$ (central velocity) is given by

$$\vec{v}^{(c)} = \lim_{c\to 0}\left(L_{xz}^{\prime(crack)}c\right)\vec{e}'_x + \lim_{c\to 0}\left(L_{yz}^{\prime(crack)}c\right)\vec{e}'_y \tag{7}$$

The second term in Eq. (6) describes the part of the velocity field that suffers a jump across the crack. The jump in the velocity is tangential to the crack surfaces and its orientation is uniform on the crack surfaces. The magnitude of the jump is at a maximum in the centre and it is zero at the crack rim. Assuming $a > b$, we find (see Appendix A)

$$\begin{aligned} v_x^{\prime(c)} &= \lim_{c\to 0}\left(L_{xz}^{\prime(crack)}c\right) \\ &= 2bD_{xz}^{\prime(\infty)}\left[E(k) + \frac{1}{(a/b)^2-1}\left\{F(k)-E(k)\right\}\right]^{-1} \end{aligned} \tag{8}$$

where $k^2 = 1 - (a/b)^{-2}$, and $E(k)$, $F(k)$ denote the complete elliptical integrals of the first and second kind (Abramowitz and Stegun, 1968).

$$E(k) = \int_0^{\frac{\pi}{2}} \frac{d\theta}{\sqrt{1-k^2\sin\theta}}, \quad F(k) = \int_0^{\frac{\pi}{2}} \sqrt{1-k^2\sin\theta}\,d\theta \tag{9}$$

In case $a < b$, the following transformations need to be applied in Eq. (8)

$$k'^2 = 1-(a/b)^2, \quad E(k)\to(b/a)E(k'), \quad F(k)\to(a/b)F(k') \tag{10}$$

resulting in

$$v_x'^{(c)} = 2aD_{xz}'^{(\infty)}\left[2E(k') + \frac{(a/b)^2}{(a/b)^2-1}\left\{F(k')-E(k')\right\}\right]^{-1} \tag{11}$$

For $a > b$, $v_y'^{(c)}$ is given by Eq. (11) after interchanging a with b and replacing $D_{xz}'^{(\infty)}$ with $D_{yz}'^{(\infty)}$. Similarly, $v_y'^{(c)}$ is obtained using Eq. (8) for $a < b$.

It is useful to normalize the components of the central velocity vector with the length of the corresponding crack axis and the corresponding resolved shear rate. We denote the normalized components as $\tilde{v}_x'^{(c)} = v_x'^{(c)}/(aD_{xz}'^{(\infty)})$ and $\tilde{v}_y'^{(c)} = v_y'^{(c)}/(bD_{yz}'^{(\infty)})$. It is sufficient to analyze just one and we show $\tilde{v}_x'^{(c)}$ as a function of the crack aspect ratio a/b in Fig. 3. In the limit of $a/b \to 0$, $\tilde{v}_x'^{(c)}$ is equal to 1. The model configuration now reproduces the 2D-models and the result is in agreement with results obtained using independent techniques (e.g. Grasemann et al., 2005; Kocher and Mancktelow, 2005; Mulchrone, 2007). The normalized component of the central velocity still yields $8/3\pi \approx 0.84$ for the penny-shaped crack ($a = b$) and it decreases like b/a for $a \gg b$. Using b instead of a in the normalization, we obtain $v_x'^{(c)}/(bD_{xz}'^{(\infty)}) \to 2$ for $a/b \to \infty$.

Using the normalized components, the central velocity takes the form

$$\vec{v}^{(c)} = \tilde{v}_x'^{(c)} aD_{xz}'^{(\infty)}\vec{e}'_x + \tilde{v}_y'^{(c)} bD_{yz}'^{(\infty)}\vec{e}'_y \tag{12}$$

For $a \neq b$, the products $\tilde{v}_x'^{(c)}a$ and $\tilde{v}_y'^{(c)}b$ yield different values. The difference results in a non-parallelism between $\vec{v}^{(c)}$ and the vector $\vec{d} = D_{xz}'^{(\infty)}\vec{e}'_x + D_{yz}'^{(\infty)}\vec{e}'_y$ that describes the direction of the far-field shear resolved on the crack surface. We introduce β to denote the angle between the two vectors, and α denotes the angle between the resolved shear $\vec{d}$ and the short semi-axis $\vec{b}$, where we take $a>b$. We show β as a function of the angle α for selected aspect ratios between 2 and 100 in Fig. 4. The central velocity $\vec{v}^{(c)}$ is always at a smaller angle to the long axis $\vec{a}$ as compared to the resolved shear $\vec{d}$. The angle β attains a maximum when the angle between $\vec{d}$ and $\vec{v}^{(c)}$ is bisected by the direction that itself bisects the x' and y' directions. At the maximum, the resolved shear vector is oriented at an angle α_{max}

$$\alpha_{max} = \tan^{-1}\sqrt{\frac{\tilde{v}_y'^{(c)}b}{\tilde{v}_x'^{(c)}a}} \le \frac{\pi}{4} \tag{13}$$

The maximal β yields

$$\beta_{max} = 2\left(\frac{\pi}{4} - \alpha_{max}\right) \tag{14}$$

For a blade-shaped inclusion ($a/b = 100$), we find β_{max} of approximately 19°.

3.2.2. External velocity field

The velocity field about the elliptical crack was obtained as a limiting case of the solution derived by Eshelby (1959). Firstly, the solution is reduced to the incompressible case, i.e. Poisson ratio is set to 1/2. Next, we set $\mu^{incl}/\mu^{host} \to 0$ and $c \to 0$. The details of the limiting procedure are omitted here. The velocity field takes the form

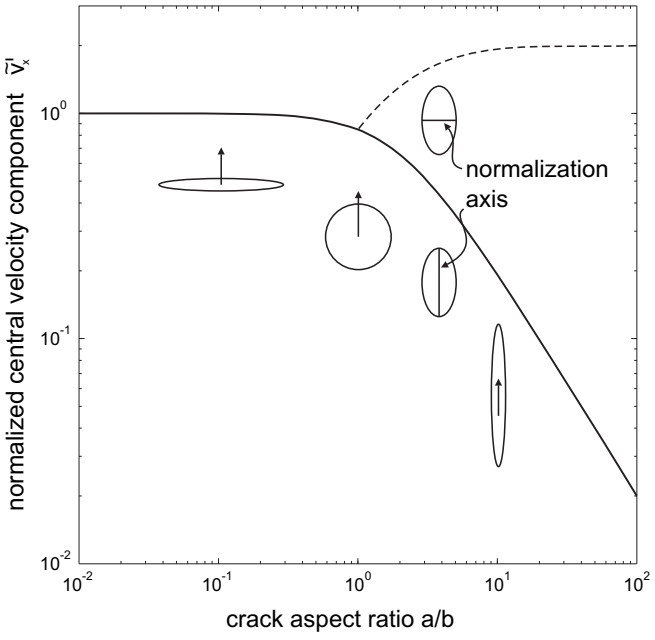

Fig. 3. Normalized central velocity component $\tilde{v}'_x$ as a function of the aspect ratio a/b. The velocity is normalized by the resolved shear rate and the length of the shear parallel axis. The dashed curved corresponds to the normalization by the length of the short axis for a crack elongated in the shear direction.

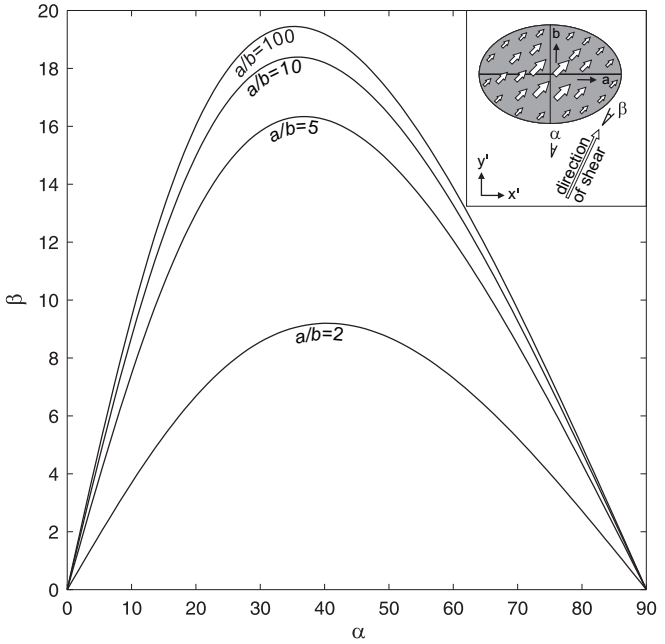

Fig. 4. Misorientation β of central velocity with respect to the resolved shear, as a function of angle α between the crack semi-axis $\vec{b}$ and the resolved shear vector $\vec{d}$, for different initial aspect ratios ($a/b = 2$, 5, 10 and 100). The misorientation increases with the aspect ratio and for $a/b = 100$, it reaches ~19°.

$$
\begin{aligned}
v'_x &= \frac{1}{4\pi}\left[v_x'^{(c)}\left(z'\frac{\partial^2\tilde{\Phi}}{\partial x'^2}-\frac{\partial\tilde{\Phi}}{\partial z'}\right)+v_y'^{(c)}z'\frac{\partial^2\tilde{\Phi}}{\partial x'\partial y'}\right]\\
v'_y &= \frac{1}{4\pi}\left[v_x'^{(c)}\left(z'\frac{\partial^2\tilde{\Phi}}{\partial x'\partial y'}-\frac{\partial\tilde{\Phi}}{\partial z'}\right)+v_y'^{(c)}z'\frac{\partial^2\tilde{\Phi}}{\partial y'2}\right]\\
v'_z &= \frac{1}{4\pi}\left[v_x'^{(c)}z'\frac{\partial^2\tilde{\Phi}}{\partial x'\partial z'}+v_y'^{(c)}z'\frac{\partial^2\tilde{\Phi}}{\partial y'\partial z'}\right]
\end{aligned}
\tag{15}
$$

where $\tilde{\Phi}$ denotes the harmonic potential Φ of a solid ellipsoid scaled upon the length c, i.e. $\Phi = c\tilde{\Phi}$. The formulas for the potential $\tilde{\Phi}$ and its derivatives can be found in the original paper of Eshelby (1959).

3.3. Crack shape in finite deformation

A homogeneous and constant velocity gradient field $\mathbf{L}^{(\infty)}$ leads to a homogeneous deformation gradient field $\mathbf{F}^{(\infty)}$

$$\mathbf{F}^{(\infty)}(t) = \exp\left(\mathbf{L}^{(\infty)}t\right) \tag{16}$$

where t denotes time. In finite homogeneous deformation the position vectors $\vec{r}$ change according to

$$\vec{r}(t) = \mathbf{F}^{(\infty)}(t)\vec{r}(0) \tag{17}$$

Since the points at the crack rim always experience the unperturbed background velocity field, their position vectors $\vec{r}^{(rim)}(t)$ are linearly dependent on the initial positions $\vec{r}^{(rim)}(0)$ through the deformation gradient $\mathbf{F}^{(\infty)}$. Hence, the shape evolution of the crack amounts to a two-dimensional stretching in the plane of the crack and rotation.

To find the current configuration of the crack, we first consider the mapping of a unit circle $\vec{r}^{(circle)}$ onto the initial positions of the points lying on the crack rim

$$\vec{r}^{(rim)}(0) = \mathbf{R}(0)\mathbf{U}(0)\vec{r}^{(circle)} \tag{18}$$

where the rotation matrix $\mathbf{R}(0)$ involves the three Euler angles $\psi_1(0),\ \varphi(0),\ \psi_2(0)$ that correspond to the initial orientation of the crack and $\mathbf{U}(0)$ is a stretch matrix with zero off diagonal elements that contains the initial axis lengths $a(0)$, $b(0)$ and $c = 0$ as its diagonal. The current position vectors of the points at the crack rim are

$$\vec{r}^{(rim)}(t) = \mathbf{F}^{(\infty)}(t)\mathbf{R}(0)\mathbf{U}(0)\vec{r}^{(circle)} \tag{19}$$

As anticipated the crack rim remains an ellipse. The crack orientation and axis lengths are found using the polar decomposition of the product of the deformation gradient tensor, and the rotation and stretch matrices

$$\mathbf{R}(t)\mathbf{U}(t) = \mathbf{F}^{(\infty)}(t)\mathbf{R}(0)\mathbf{U}(0) \tag{20}$$

where $\mathbf{R}(t)$ describes the current orientation, and the current axis lengths are on the diagonal of $\mathbf{U}(t)$. The three Euler angles $\psi_1(t), \varphi(t), \psi_2(t)$ can be determined from $\mathbf{R}(t)$.

3.4. Offset

The offset vector $\vec{r}^{(c)}(t) = x'^{(c)}(t)\vec{e}'_x(t) + y'^{(c)}(t)\vec{e}'_y(t)$ connects the crack center to the particle initially above it. The rate of offset vector is equal to the velocity of this particle as it moves along the crack surface

$$\dot{\vec{r}}^{(c)} = \mathbf{L}^{(\infty)}\vec{r}^{(c)} + \vec{v}^{(c)}\sqrt{1-\left(x'^{(c)}/a\right)^2-\left(y'^{(c)}/b\right)^2} \tag{21}$$

The offset is primarily due to the jump in the velocity given by the second term of Eq. (21). At sufficiently large offset, the contribution of the first term may predominate as the magnitude of the velocity jump decreases towards the crack rim.

4. Flanking structures in 3D

4.1. Monoclinic flanking structures

We consider the special case, where the crack axis $\vec{b}$ is parallel to the fixed axis $\vec{y}$ during deformation. The latter one corresponds to an intermediate axis in pure shear flow (Eq. (1)) and an axis that is orthogonal to the shear direction within the shear plane in simple shear flow (Eq. (2)). The second Euler angle φ gives the angle between the crack axis $\vec{a}$ and the fixed axis $\vec{x}$ and we refer to it as the inclination. The other two Euler angles are equal to zero. The length of the crack axis $\vec{b}$ is constant. The structure forming around the crack is characterized by a monoclinic symmetry due to the symmetry of the background flow and the orientation of the crack with respect to the principal flow axes.

If one of the crack axis and the resolved shear vector remain parallel during the deformation, Eq. (21) can be simplified. The rate of change of $x'^{(c)}$is now given by

$$\dot{x}'^{(c)} = v_x'^{(c)}\sqrt{1-\left(\frac{x'^{(c)}}{a}\right)^2}+x'^{(c)}\frac{\dot{a}}{a} \tag{22}$$

where $\dot{a}/a = L'^{(\infty)}_{xx}$. Dividing by a and rearranging, we obtain

$$\frac{\dot{x}'^{(c)}}{a}-x'^{(c)}\frac{\dot{a}}{a^2} = \frac{v_x'^{(c)}}{a}\sqrt{1-\left(\frac{x'^{(c)}}{a}\right)^2} \tag{23}$$

The left hand side of Eq. (23) is the rate of a normalized offset $x'^{(c)}/a$. Introducing $\tilde{x}'(c) = x'(c)/a$, moving the radical to the left hand side and using the normalized central velocity, we obtain

$$\frac{\dot{\tilde{x}}'^{(c)}}{\sqrt{1-\left(\tilde{x}'^{(c)}\right)^2}} = \frac{\mathrm{d}}{\mathrm{d}t}\arcsin\left(\tilde{x}'(c)\right) = \tilde{v}_x'^{(c)}D'^{(\infty)}_{xz} \tag{24}$$

The central velocity $\tilde{v}_x'^{(c)}$ depends on the crack aspect ratio, and the resolved shear $D'^{(\infty)}_{xz}$ depends on crack orientation. Integrating the normalized offset incorporates the contribution from the inclusion deformation to the offset accumulation.

The velocity jump is vanishing in the y-direction and for an arbitrary point on the crack surface, Eq. (22) takes the form

$$\dot{x}' = v_x'^{(c)}\sqrt{1-\left(\frac{x'}{a}\right)^2-\left(\frac{y'}{b}\right)^2}+x'\frac{\dot{a}}{a} \tag{25}$$

Following similar transformations as in Eq. (23) and Eq. (24) and introducing an apparent crack axis length $a^* = a\sqrt{1-(\frac{y'}{b})^2}$, we obtain

$$\frac{\mathrm{d}}{\mathrm{d}t}\arcsin\left(\tilde{x}'\right) = \tilde{v}_x'^{(center)}D'^{(\infty)}_{xz} \tag{26}$$

where $\tilde{x}' = x'/a^*$, i.e. the normalization is performed using the apparent axis length that is determined by a constant y'. The result shows that the normalized separation of initially central pairs of points remains constant for all xz-sections for a monoclinic flanking structure. In this case, using the normalized offset allows incorporating not only the effect of the crack stretching, but also the effect of analyzing the structure on different sections parallel to the stretching or shearing direction.

4.1.1. Monoclinic flanking structures in pure shear

In pure shear (Eq. (1)), the resolved shear rate $D'^{(\infty)}_{xz}$ yields

$$D'^{(\infty)}_{xz} = \frac{D^{(\infty)}_{zz} - D^{(\infty)}_{xx}}{2}\sin 2\varphi = -D^{(\infty)}_{xx}\sin 2\varphi \tag{27}$$

The rate of inclination of a passive line is now equal to $D^{(\infty)}_{xx}\sin 2\varphi$. Using inclination rather than time as a variable of integration in Eq. (24), we obtain

$$[\arcsin(s)]_0^{\tilde{x}'_0} = -\int_{\varphi^{init}}^{\varphi} \tilde{v}'^{(c)}_x \mathrm{d}\varphi' \tag{28}$$

Letting $a/b \to 0$ (2D limit), the normalized x-component of the central velocity $\tilde{v}'^{(c)}_x$ becomes **1** and the normalized offset yields

$$\tilde{x}'^{(c)} = -\sin(\Delta\varphi) \tag{29}$$

where $\Delta\varphi = \varphi - \varphi^{init}$. Thus, the normalized offset now depends exclusively on the difference between the inclinations, irrespective of the initial inclination. The sine function in Eq. (29) appears due to the velocity decaying with an increasing offset. The central point can only reach the crack tip for the inclination change $\Delta\varphi$ approaching 90°, i.e. if the crack axis $\vec{a}$ is initially subparallel to the shortening direction $\vec{z}$.

The normalized central velocity depends on the crack aspect ratio, and it is strongly reduced for $a > b$ as shown in Fig. 3. The evolution of the crack aspect ratio is described by

$$a/b = (a/b)_0\sqrt{\cosh\left[D^{(\infty)}_{xx}t\right]} \tag{30}$$

where $(a/b)_0$ is the reference aspect ratio at the reference orientation of $\varphi_0 = 45°$ ($t = 0$). We note that a/b is a symmetric function about $t = 0$ and the reference value $(a/b)_0$ is a global minimum. Upon numerical integration, the normalized offset can be found for an arbitrary initial aspect ratio and inclination. For a finite crack aspect ratio, the normalized offset depends on φ^{init} in addition to $\Delta\varphi$.

As an example, Fig. 5a shows the marker deflection and offset for different values of the reference aspect ratio $(a/b)_0$, at an identical length of the axis $\vec{a}$ and initial inclination $\varphi^{init} = 70°$. The simulation was run until $\Delta\varphi = 50°$. The normalized offset is ~0.77 for $a/b \to 0$. For $(a/b)_0 = 10$, the normalized offset yields 0.18 and it is related to a significantly weaker deflection of the marker.

4.1.2. Monoclinic flanking structures in simple shear

In a simple shear flow given by Eq. (2), the inclination changes according to

$$\cot\varphi = \cot\varphi^{init} - 2D^{(\infty)}_{xz}t \tag{31}$$

leading to

$$\frac{\mathrm{d}\varphi}{\mathrm{d}t} = 2D^{(\infty)}_{xz}\sin^2\varphi \tag{32}$$

We note that the rate of inclination is positive for all $\varphi \in (0, 180°)$ and crack axis $\vec{a}$ rotates towards the shearing direction that is parallel to the axis $\vec{x}$ ($\varphi = 180°$).

The velocity jump can be either synthetic or antithetic to the rotation of the crack, depending on its inclination (Grasemann et al., 2003). The resolved shear rate $D'^{(\infty)}_{xz}$ is equal to $D^{(\infty)}_{xz}\cos 2\varphi$. Therefore, the central velocity is positive and the velocity jump is synthetic to the crack rotation for $\varphi \in (0, 45°) \cup (135°, 180°)$. As the sign of the central velocity changes, previously accumulated offset may be reduced or even inverted (Exner et al., 2004).

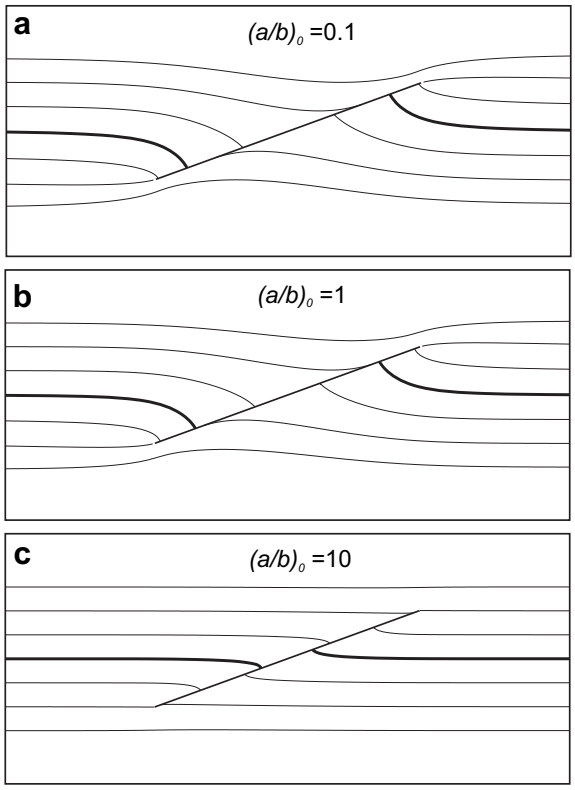

Fig. 5. Pure shear experiments with $\varphi_{init} = 70°$, $\varphi_{final} = 20°$ and for different aspect ratios $(a/b)_0$ (defined at $\varphi_0 = 45°$).

In the 2D-case ($a/b \to 0$), the central velocity is constant and equal to 1 resulting in

$$[\arcsin(s)]_0^{\tilde{x}'_0} = \frac{1}{2}\int_{\varphi^{init}}^{\varphi} \frac{\cos 2\varphi'}{\sin^2\varphi'}\mathrm{d}\varphi' \tag{33}$$

The normalized offset as a function of inclination is given by

$$\tilde{x}'_0 = \sin\left[\left(-\frac{1}{2}\cot\varphi - \varphi\right)\Big|_{\varphi^{init}}^{\varphi}\right] \tag{34}$$

Using Eq. (31) in Eq. (34), we can express the offset as a function of time rather than inclination. In simple shear, the offset cannot be expressed solely in terms of the inclination difference $\Delta\varphi$ as it is in the pure shear case.

As an example, we investigate a simple shear flow up to shear strain $\gamma = 2D^{(\infty)}_{xz}t = 14$ using an initial crack inclination of $\varphi^{init} = 45°$ (Fig. 6). The axis $\vec{a}$ is first subject to shortening until it reaches $\varphi = 90°$ ($\gamma = 1$). As it is subsequently stretching, the crack aspect ratio is now at a minimum that we use as the reference value $(a/b)_0$. For $\varphi \in (45°, 90°)$, the central marker is partly duplicated along the crack and the offset can be described as contractional. At $\varphi = 90°$, the offset becomes extensional, i.e. the central marker is partly missing along the crack. The offset is accumulated due to a negative velocity jump up to $\varphi = 135°$ ($\gamma = 2$). As the crack inclination reaches 135° at $\gamma = 2$, the offset attains a minimum (Fig. 7a–c). The minimal normalized offset for $a/b \to 0$ yields $-\cos(1) \approx -0.54$. For $(a/b)_0 = 10$, the minimum offset yields only −0.14.

The velocity jump changes the sign at $\varphi = 135°$ and the previously accumulated offset is reduced until it vanishes at a certain strain that we refer to as the transition strain. The transition strain depends on the reference aspect ratio $(a/b)_0$ (Fig. 7d–f). For

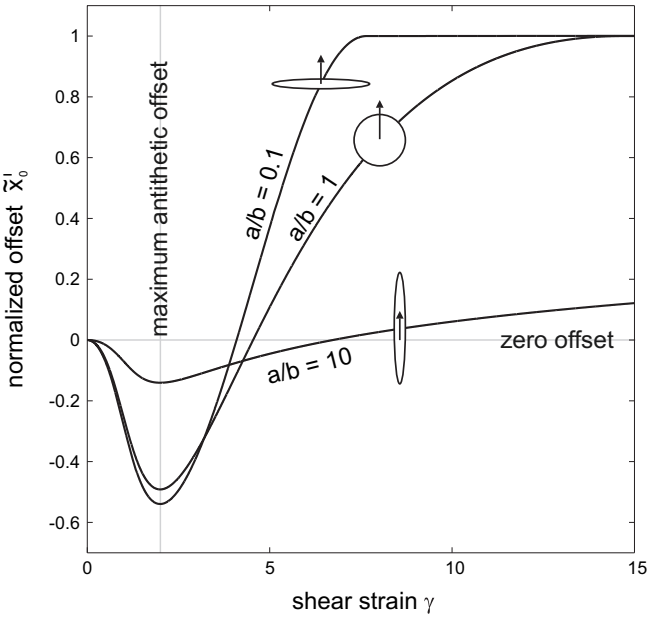

Fig. 6. The evolution of normalized offset $\tilde{x}_0'$ with shear strain γ is shown for three selected reference aspect ratios $(a/b)_0$, corresponding to Fig. 6. The minimum offset (maximum antithetic offset) is reached at $\gamma = 2$, irrespective of $(a/b)_0$, but the magnitude of offset differs dramatically and evolves unequally for different aspect ratios. Synthetic offset is accumulated until the markers are pinned at the crack tips (at $\tilde{x}_0' = 1$) and no further offset is accommodated.

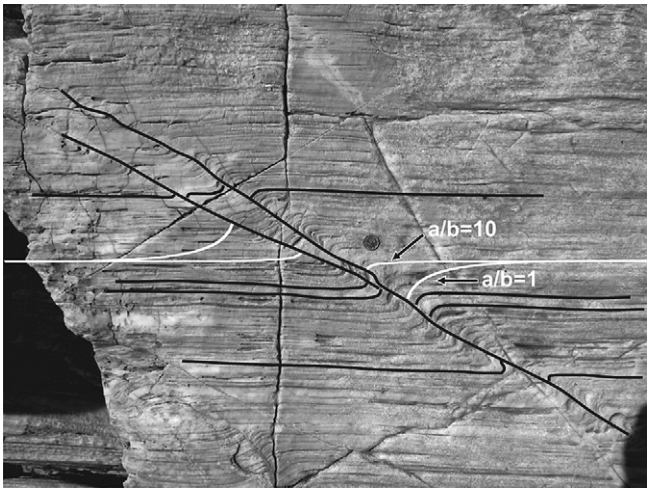

Fig. 8. Flanking structure in banded marble on Naxos, Greece, where the width of deflection extends $<a/16$ laterally from the crack. For comparison, the marker geometries for $a/b = 1$ and $a/b = 10$ are plotted as white lines, using an initial length of a slip line identical to the one seen in the picture. The width of deflection of the natural structure is closer to the geometry of $a/b = 10$, suggesting a high aspect ratio of the crack (with $a > b$; compare to Fig. 6a).

$a/b \to 0$, it is given by a root of $tan(x/2 - \pi/4) - x + 1 = 0$ yielding $\sim$4.1. For a finite crack aspect ratio, the transition occurs at a higher strain. The effect is due to a reduced velocity jump as the axis length a is increasing and a reduced resolved shear rate $D_{xz}^{\prime(\infty)}$ as the crack rotates towards the shear plane.

For $\varphi > 135°$, the offset becomes contractional (compare to fig. 6 of Exner et al., 2004). The maximum synthetic offset is limited by the length a. For $a/b \to 0$, the normalized offset reaches 1 at $\gamma \approx 7.5$ indicating that the central point collapses onto a point at the crack tip. For the penny shape inclusion case $(a/b)_0 = 1$, it takes $\gamma \approx 14$ for the collapse to happen.

The structure formed around the crack for $(a/b)_0 = 10$ is significantly different than the structure for $(a/b)_0 \leq 1$. The width of the zone where the initially planar markers are significantly deflected around the inclusion is dependent on the crack aspect

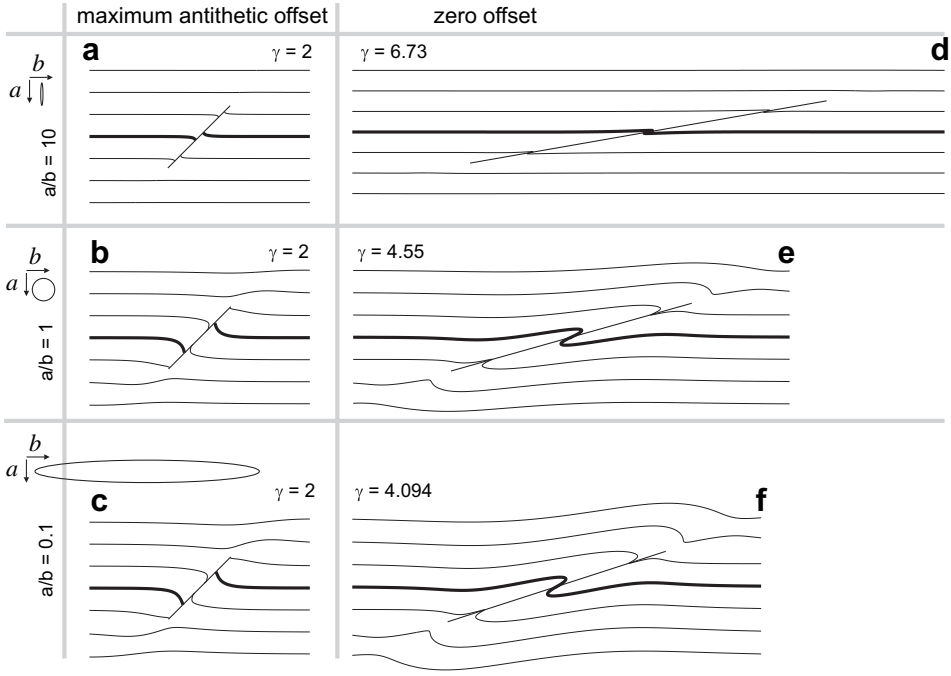

Fig. 7. The two-dimensional deflection geometry and offset as a function of the reference aspect ratio of the crack $(a/b)_0$, as demonstrated on three examples in two stages (with common $\varphi_0 = 45°$). The left column depicts the stage of the maximum antithetic offset at $\gamma = 2$. Note that at $\gamma = 2$ for $(a/b)_0 = 10$, the magnitude of offset is significantly lower than in (b) and (c); likewise, the zone of deflection is more narrow. The right column shows the structure captured at a shear strain when the offset is again decreased to zero.

ratio. In Fig. 7c, the deflection extends much further away from the crack for $(a/b)_0 \leq 1$ than in the experiment with $(a/b)_0 = 10$ (Fig. 7a), which is also observed in the natural example of Fig. 8.

In Fig. 9a, we observe the development of isoclinal folds with limbs subparallel to the crack plane around $\gamma = 7$. Asymmetric isoclinal folds are located beyond the inclusion tips, while the center of the structure is dominated by markers parallel to the crack plane that is now at a low angle to the shear plane. Once the central marker is displaced up to the crack tips, no further offset can be accumulated, while the associated folds are continuously sheared and thereby passively amplified. Similar structures are found in natural examples (Fig. 9b).

These folds strongly resemble sheath folds (Fig. 9c), which are characterized by curved fold axes and non-cylindrical shapes (e.g. Cobbold and Quinquis, 1980; Alsop and Holdsworth, 2004). As the semi-axis $\vec{a}$ was stretched while the semi-axis $\vec{b}$ retained a constant length, the crack aspect ratio changed from the initial value 0.1 to >2 at $\gamma = 7$. Thus, the structure evolves from a quasi-cylindrical to a strongly non-cylindrical flanking fold geometry.

4.2. Triclinic flanking structures

We analyze a more general setup, where the crack axis $\vec{b}$ is initially oriented within the shear plane (xy), but at an angle $\psi_1 \neq 0^\circ$ to the y-direction. An oblique initial orientation results in a re-orientation of the principal axes of the crack during deformation. This effect influences the amount and sense of offset. A non-vanishing ψ_1 results in a non-zero y-component of the resolved shear vector leading to the displacement of the marker lineation perpendicular to the xz-plane. The misorientation

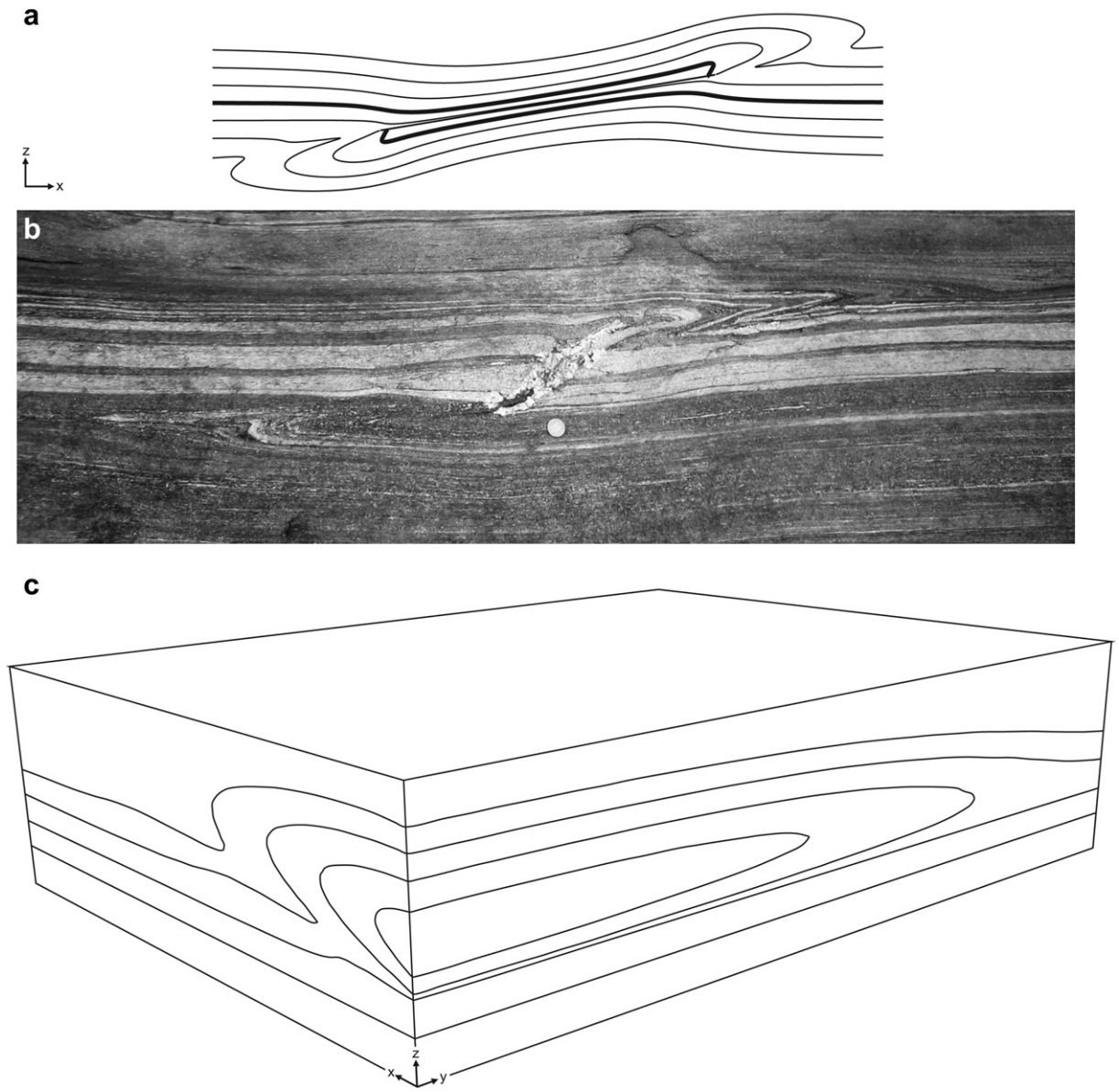

Fig. 9. (a) Experimental result for a structure initiated at $\varphi_0 = 45^\circ$ with $a/b = 0.1$, developed in dextral simple shear at $\gamma = 7$. Note that the central marker is displaced nearly up to the crack tips, and oriented largely parallel to the crack. Prominent, asymmetric tight folds are developed beyond the crack tips. (b) Potential natural example of flanking structure with low initial aspect ratio ($a/b \sim 0.1$, potentially corresponding to the model in (a)). (c) Oblique view to the structure in (a), cut parallel to the xz and yz-planes, displaying the typical eye-shaped fold of a sheath fold along the yz-section.

between the central velocity and the resolved shear vector may introduce an additional deflection of markers perpendicular to the *xz*-plane.

4.2.1. Triclinic flanking structures in simple shear

We compare structures developed about elliptical cracks in simple shear ($\gamma = 3$), with different non-zero initial orientations ψ_1^{init}but an identical initial aspect ratio $(a/b)_{\text{init}} = 1$ and an identical initial dihedral angle between the crack plane and the shear plane $\varphi^{init} = 150^\circ$ (Fig. 10). For comparison, Fig. 10a shows a monoclinic flanking structure, where $\psi_1 = 0^\circ$. For $\psi_1 \neq 0^\circ$, the crack axis $\vec{b}$ rotates away from $\vec{\chi}$ increasing the third Euler angle ψ_2. The orientation of the line of nodes $\vec{\chi}$ is unchanged and the angle ψ_1 remains constant. The final value of ψ_2 decreases with $\psi_1 = \psi_1^{init}$. The rate of the dihedral angle φ is smaller for lower ψ_1^{init}.

The crack aspect ratio and orientation as well as the surrounding structure differ significantly for different ψ_1^{init}. Already at $\psi_1 = 15^\circ$, a slight deviation from monoclinic symmetry (as in Fig. 10a) is documented by the elevation contours of the deflected marker close to the inclusion; this effect becomes more prominent with increasing ψ_1 in Fig. 10c and d, where a triclinic symmetry of deflected linear and planar markers in the *xy*-plane is evident. Nevertheless, *xz*-sections through the crack center still exhibit monoclinic symmetry (upper right corner in Fig. 10a–d).

In natural shear zones, the identification of triclinic flanking structures may be challenging, as three-dimensional exposures are rare. Nevertheless, several reliable examples encourage applying the modeling results to estimate kinematic boundary conditions and initial orientation. Several dozens of flanking structures (Fig. 1b) are exposed on a foliation plane of mylonitic orthogneiss on the island of Serifos, Greece (Iglseder et al., 2009). The structures are interpreted as upper greenschist facies reactivation of an earlier joint system oriented at $\varphi \sim 30^\circ$ to the mylonitic foliation, and show relatively consistent geometrical features regarding their size of several cm in length and offset of the mylonitic foliation by 1–5 cm along their dip. The strike of the whole population is consistently oblique to a prominent mineral lineation ($\| x$), at $\psi_2 \sim 60^\circ$, their dip orientation relative to the mylonitic foliation lies within a broader range ($\varphi \sim 135$–165°). Inferring simple shear background flow conditions from the constant value of ψ_2, and using the orientation of the precursor joints as initial orientation, we constrain the finite shear strain for these structures to $\gamma \sim 2.5$ (Fig. 1b).

4.2.2. Triclinic flanking structures in pure shear

The experiments shown in Fig. 11 are set up with an identical initial condition of $\varphi = 80^\circ$, $\psi_1^{init} = 60^\circ$ and $(a/b)^{\text{init}} = 1$, but run under either simple or pure shear of the same rate. Both structures show a triclinic symmetry, most prominently traced by the lateral deflection of the marker lineation, but also by the elevation of the marker planes. In detail: (1) The lateral offset (in *y*-direction) of linear markers is sinistral in simple shear, but dextral in pure shear. (2) The crack aspect ratio a/b is >1 in

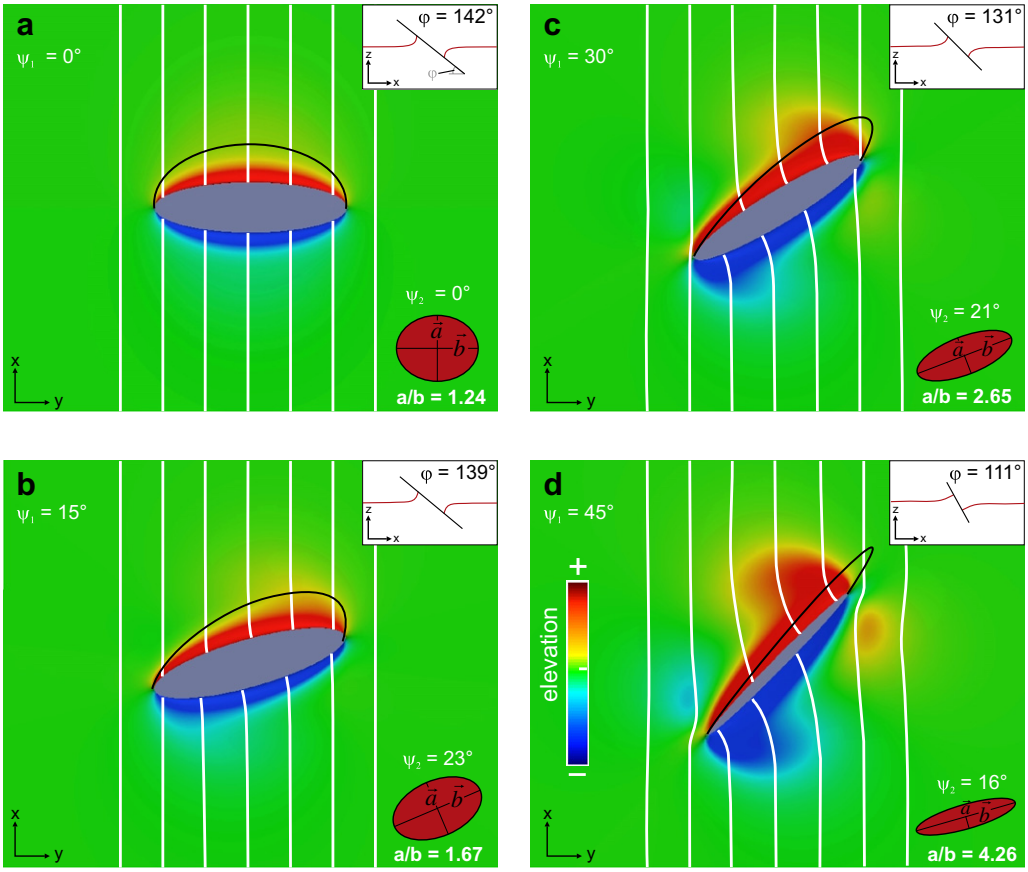

Fig. 10. Four different experiments of 3D flanking structures with different initial angles ψ_1^{init} (0, 15, 30 and 45°) between the crack semi-axis $\vec{b}$ and the *y*-axis. All experiments have identical initial aspect ratio ($a/b = 1$) and the two remaining Euler angles ($\varphi^{init} = 30^\circ$, $\psi_2^{init} = 0$), and finite simple shear strain ($\gamma = 3$). The structures deviate in finite rotation and stretch of the crack (φ and ψ_2 angles and aspect ratio a/b), offset of markers in both *xz*-plane (cross section in upper right corner of each figure), and parallel to the *y*-direction (white linear markers), and deflection of marker planes (elevation contours). Note that the initial angles ψ_1^{init} are not modified during simple shear deformation.

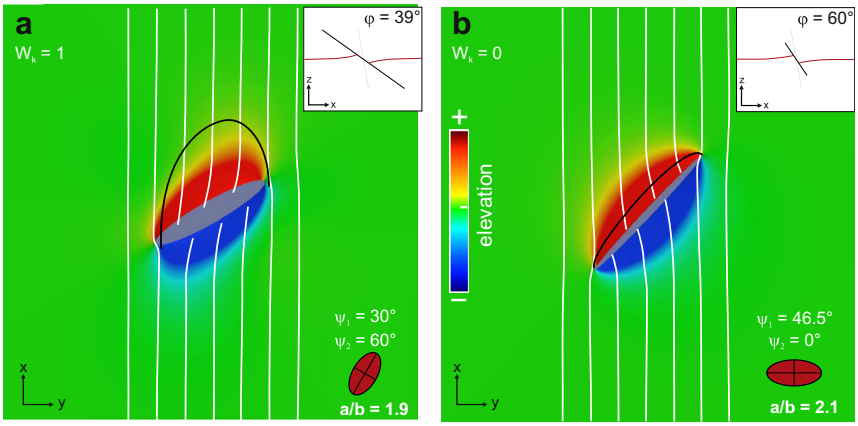

Fig. 11. Two experiments with identical initial conditions ($\psi_1^{init} = 30°$, $\varphi^{init} = 80°$, $a/b = 1$) run at simple shear $\gamma = 1.2$ (a) and pure shear of an identical magnitude (b) background flow. Finite structures differ in finite aspect ratio a/b, orientation to xy-plane (φ-angle), offset of marker plane and deflection geometry (highlighted by color contours of elevation). While in simple shear, the angle ψ_1 remains constant, it is increased to 46.5° in pure shear. The angle ψ_2 changes to a value of 60° in simple shear, but remains zero in pure shear. Note that the offset of the maker lineation is left-lateral in simple shear and right-lateral in pure shear and that φ-angles are depicted as apparent angles along xz-sections. The lateral magnitude of offset is higher than the vertical offset in pure shear (For interpretation of the references to colour in this figure legend, the reader is referred to the web version of this article).

simple shear, but <1 in pure shear. (3) Counter-clockwise rotation of the crack around the z-axis reduces the angle ψ_1 by 16.5° in pure shear, while this angle remains unaltered in simple shear. (4) The final orientation of the crack axis $\vec{a}$ is by 20° lower in simple shear, due to a higher rotation rate in comparison with pure shear. (5) The angle of $\psi_2 = 0°$ remains constant in pure shear, indicating that the axis $\vec{b}$ is not rotated out of the xy-plane. The crack axes are only stretched and rotated into the direction of the x-axis (thereby reducing ψ_1), but not reoriented with respect to the axis $\vec{c}$ as they are in simple shear. In summary, a clear distinction can be made between pure shear and simple shear scenarios.

We identified a natural example which displays the characteristic geometrical features of a triclinic flanking structure developed in pure shear boundary conditions from an amphibolite mylonite on Serifos, Greece (Fig. 1d). The structure is oriented at $\psi_1 = 55°$ to the mineral lineation, at a steep angle to the mylonitic foliation plane ($\varphi \sim 70°$). Strikingly, the left-lateral offset of linear markers and associated deflection is larger than the down-dip displacement along the discontinuity. This observation is in accordance with experiments in pure shear background conditions, where lateral offset exceeds down-dip displacement. Furthermore, the population of flanking structures observed in this outcrop records variable angles with respect to the mineral lineation (ψ_1). Thus, pure shear flow conditions, or more cautiously pure shear dominated general shear may be inferred for the formation of this population 3D flanking structures.

5. Discussion

5.1. Estimating the aspect ratio of a crack

Two-dimensional studies of flanking structures using analogue, numerical or analytical models conveniently assume that the structures are largely cylindrical. In contrast, we demonstrate that the finite length of the crack perpendicular to a flow plane may influence the velocity jump and thus the finite geometry significantly. This finding offers the potential to estimate the aspect ratio of a roughly elliptical crack from geometrical observations on 2D-sections, ideally oriented parallel to a corresponding stretching lineation and perpendicular to a foliation plane. Certainly, the exact orientation and position might be difficult to establish in the field, and certain geometries may be interpreted in several ways. As an example, a small offset may be interpreted as (1) a low aspect ratio and system captured at some particular strain (e.g. zero offset in Fig. 7f), or (2) a high aspect ratio. Nevertheless, we argue that (1) is statistically unlikely, which leaves a high aspect ratio as the most likely scenario that can be corroborated by the presence of small amplitude deflections. Apart from that, a significant offset recorded along a crack with respect to its length indicates that the crack is elongated perpendicular to the flow plane.

Comparing the experimental geometries in Fig. 7a with the natural example in Fig. 8 gives us confidence that a first order estimate of the crack aspect ratio can be made from simple geometrical relationships observed in the field. In this example, the disproportionately narrow zones of deflection are not reproducible with 2D-models, and suggest a high aspect ratio of the crack. In contrast, peculiar features like isoclinal folds beyond the tips of the crack (Fig. 9) can be reproduced in 2D-models, indicating a low aspect ratio of the crack. However, such conclusion must be evaluated cautiously, as anisotropic host material may change the slip rate significantly (Kocher and Mancktelow, 2006; Fletcher, 2009).

We emphasize that 2D plane strain models may only be valid for cracks where the longest axis is oriented perpendicular to the shear vector. Examples where low aspect ratios ($a/b < 0.1$) of the crack are well constrained are suitable for a determination of the kinematic vorticity number of the shear zone from the geometry of flanking structures (Kocher and Mancktelow, 2005; Gomez-Rivas et al., 2007); otherwise, strain and kinematic reconstructions from 2D-sections may lead to erroneous conclusions.

5.2. Sheath folds

The experiments using a low initial crack aspect ratio ($a/b = 0.1$) produce isoclinal folds beyond the inclusion tips at shear strains of $\gamma = 7$ in simple shear (Fig. 9). As the aspect ratio is progressively increasing by stretching of the crack's axis $\vec{a}$, the resulting 3D-structure develops a strongly non-cylindrical geometry, reflected by curved fold hinges of the isoclinal folds.

Generally, such fold geometries are described as tubular or sheath folds (e.g. Cobbold and Quinquis, 1980; Alsop and Holdsworth, 2004). To our knowledge, only the development of sheath folds around rigid inclusions has been recognized so far (e.g. Marques and Cobbold, 1995; Rosas et al., 2002), but no similar observations or experiments are reported for weak inclusions. In natural shear zones, a strongly sheared vein or other weak object subparallel to an adjacent marker layer could be difficult or impossible to identify, leaving the associated folds unrelated to any obvious vein or crack, which is mostly the case in documented natural examples of sheath folds. In our models, the flow perturbation around a crack leads to the formation of sheath folds, avoiding the necessity of an initial finite amplitude perturbation of layers or even a perturbation of fold hinges, as in other concepts for the formation of sheath folds (e.g. Alsop and Holdsworth, 2004; Mandal et al., 2009). However, our model only considers the formation of sheath folds in a kinematic manner, i.e. in a mechanically homogeneous matrix, so there is no mechanical instability.

In Fig. 9, we show a potential natural example of a sheath fold developed around a vein, exposed along a *xz*-section (where the typical eye-shaped structure cannot be observed). In addition, the same outcrop hosts several other flanking structures, which do not display tight folds beyond the vein or crack tips. Thus, we speculate that the different flanking structure geometries reflect differences in initial aspect ratio of the veins.

5.3. Inferring strain and flow kinematics from triclinic flanking structures

We modeled some few selected cases of flanking structures in monoclinic flow, where the initial oblique orientation of the elliptical crack promotes the development of structures with triclinic symmetry (Figs. 10 and 11). Applying the experiment results to field data of orientation and shape of several triclinic flanking structures (Fig. 1b and 1d), we are able to estimate flow conditions and strain recorded by the structures.

Notably, none of our experiments use triclinic flow boundary conditions, i.e. a flow type where the vorticity vector is oriented oblique to the instantaneous stretching axes (Passchier, 1997). To our knowledge, observations of triclinic structures in monoclinic flow have not been reported so far, while theoretical considerations on the variability of triclinic flow types and their likelihood in natural shear zones lack well-documented natural examples (e.g. Jiang and Williams, 1998; Iacopini et al., 2007). In field studies, triclinic transpression zones are identified by lineations with opposing plunge occurring in a single shear zone (e.g. Lin and Jiang, 2001; Sullivan and Law, 2007), where deformation is partitioned between pure and simple shear dominated domains.

The natural examples of triclinic flanking structures presented here develop in special, but well-documented initial condition, where an earlier shear zone and lineation is overprinted at an angle of ca. 30° by a new shearing event. By oblique reactivation of preexisting joints, triclinic structures may form in monoclinic simple shear (Fig. 1b) or pure shear (Fig. 1d), as shown by corresponding numerical experiments (Figs. 10 and 11). Certainly, our results do not rule out the existence of triclinic shear zones, but propose an alternative explanation for the generation of triclinic structures.

6. Conclusions

We reduce the internal and external Eshelby solution to the case of an inviscid elliptical crack to investigate the geometry of flanking structures in three dimensions. Our modeling results lead to the following conclusions:

1) The velocity jump is at maximum at the crack center and decreases to zero at the crack tips with elliptical iso-contours. The magnitude of the jump is related to the aspect ratio of the crack. When the long axis is parallel to the resolved shear direction, the central velocity jump normalized by the length of the shear parallel axis and the resolved shear rate may become significantly smaller than the reference value of one observed in two-dimensional models. The central velocity jump normalized upon the shorter of the axes is of a similar order for all aspect ratios.
2) The direction of the velocity jump is constant on an elliptical crack. If the resolved shear vector is not parallel to any of the crack axes, the direction of the velocity jump may deviate up to max. 19° from the direction of the resolved shear.
3) If subjected to homogeneous background flow, an elliptical crack exhibits the same rotation and stretching behavior as a passive material ellipse with identical aspect ratio and orientation.
4) Large strain experiments produce strongly non-cylindrical structures with curved fold hinges, suggesting that sheath folds may be formed around cracks or weak veins in simple shear dominated shear zones.
5) Shearing along an elliptical cracks oriented oblique to the principal directions of a monoclinic flow can produce triclinic structures, without necessarily imply triclinic background flow kinematics. Triclinic flanking structures may be used to estimate flow kinematics.

Acknowledgements

This study was funded by the Austrian Science Fund (FWF projects T325-N14 and V151-N22) and by a Center of Excellence grant from the Norwegian Research Council to PGP. We appreciate critical comments and support form B. Grasemann, D. Schmid and S. Martel. E. Draganits provided a hand specimen of monoclinic 3D flanking structures (Fig. 1a). Reviews by D. Iacopini and R. Fletcher substantially improved the quality of the manuscript.

Appendix A. Reduction of the Eshelby's solution to an inviscid elliptical crack

The Eshelby solution provides the displacement field inside (Eshelby, 1957) and outside (Eshelby, 1959) an ellipsoidal homogeneous inclusion whose elastic properties differ from those of the surrounding isotropic matrix. Setting the Poisson ratio to 1/2, replacing shear modulus of each material by its viscosity, and treating displacement as velocity yields the solution for the corresponding problem for a viscous inclusion in a viscous matrix (e.g. Freeman, 1987).

The inclusion rate of deformation $\mathbf{D}^{(incl)}$ and vorticity tensor $\mathbf{W}^{(incl)}$ are constant and linearly dependent on the far-field rate of deformation $\mathbf{D}^{\infty}$ and $\mathbf{W}^{\infty}$. Here, our goal is to derive $\mathbf{D}^{(incl)}$ and $\mathbf{W}^{(incl)}$ as a function of $\mathbf{D}^{\infty}$ and $\mathbf{W}^{\infty}$ in the limit of an elliptical, i.e. $c \to 0$, and inviscid inclusion, i.e. $m = \mu^{incl}/\mu^{host} \to 0$. We use the index notation and the lengths of the inclusion axes is denoted by a_1, a_2, a_3 rather than a, b, c. Throughout the analysis, we conveniently assume $a_1 > a_2 > a_3$.

The components (here we use $i, j = 1, 2, 3$) of the inclusion rate of deformation tensor $\mathbf{D}^{(incl)}$ are

$$
\begin{aligned}
D_{11}^{incl} &= \{D_{11}^{\infty}[1+(m-1)(S_{2222}-S_{2233})] - D_{22}^{\infty}[(m-1)(S_{1122}-S_{1133})]\}/K \\
D_{22}^{incl} &= \{D_{22}^{\infty}[1+(m-1)(S_{1111}-S_{1133})] - D_{11}^{\infty}[(m-1)(S_{2211}-S_{2233})]\}/K \\
D_{33}^{incl} &= -D_{11}^{incl} - D_{22}^{incl} \\
D_{ij}^{incl} &= \frac{D_{ij}^{\infty}}{1+2(m-1)S_{ijij}}, \quad for\ i \neq j
\end{aligned}
\tag{35}
$$

where

$$
\begin{aligned}
K = {} & 1+(m-1)(S_{2222}+S_{1111}-S_{2233}-S_{1133}) \\
& +(m-1)^2(S_{1111}S_{2222}-S_{1111}S_{2233}-S_{2222}S_{1133} \\
& -S_{1122}S_{2211}+S_{1133}S_{2211}+S_{1122}S_{2233})
\end{aligned}
\tag{36}
$$

and the Eshelby tensor S for the Poisson ratio set at 1/2 yields

$$
S_{iijj} = \frac{3}{4\pi}a_j^2 I_{ij}, \quad S_{ijij} = \frac{3}{8\pi}\left(a_i^2+a_j^2\right)I_{ij} \quad \text{(no summation)} \tag{37}
$$

where the symbols I_{ij} denote

$$
\begin{aligned}
I_{ij} &= (I_j - I_i)/3\left(a_i^2 - a_j^2\right) \quad i \neq j \\
I_{ii} &= \frac{4\pi}{3a_i^2} - \sum_{i \neq j} I_{ij}
\end{aligned}
\tag{38}
$$

The symbols I_i represent certain surface integrals (see Eshelby (1959) and Mura (1987) for more details), which can be expressed by the standard incomplete elliptic integrals

$$
\begin{aligned}
I_1 &= \frac{4\pi a_1 a_2 a_3}{(a_1^2-a_2^2)(a_1^2-a_3^2)^{1/2}}[F(\theta,k) - E(\theta,k)] \\
I_3 &= \frac{4\pi a_1 a_2 a_3}{(a_2^2-a_3^2)(a_1^2-a_3^2)^{1/2}}\left[\frac{a_2(a_1^2-a_3^2)^{1/2}}{a_1 a_3} - E(\theta,k)\right] \\
I_2 &= 4\pi - I_1 - I_3
\end{aligned}
\tag{39}
$$

$$
\lim_{a_3\to 0} I_1 = 0, \quad \lim_{a_3\to 0} I_2 = 0, \quad \lim_{a_3\to 0} I_3 = 4\pi \tag{43}
$$

and for I_{ij}

$$
\begin{aligned}
&\lim_{a_3\to 0} I_{12} = 0, \quad \lim_{a_3\to 0} I_{13} = \frac{4\pi}{3a_1^2}, \quad \lim_{a_3\to 0} I_{23} = \frac{4\pi}{3a_2^2} \\
&\lim_{a_3\to 0} I_{11} = 0, \quad \lim_{a_3\to 0} I_{22} = 0, \quad \lim_{a_3\to 0} a_3^2 I_{33} = \frac{4\pi}{3}
\end{aligned}
\tag{44}
$$

Upon substitution of Eq. (44) into Eq. (37), the non-zero components of the Eshelby tensor **S** and tensor Π are obtained

$$
\begin{aligned}
&\lim_{a_3\to 0} S_{3311} = \lim_{a_3\to 0} S_{3322} = 1 \\
&\lim_{a_3\to 0} S_{1313} = \lim_{a_3\to 0} S_{2323} = \tfrac{1}{2} \\
&\lim_{a_3\to 0} \Pi_{1313} = \lim_{a_3\to 0} \Pi_{2323} = \tfrac{1}{2}
\end{aligned}
\tag{45}
$$

For a finite viscosity ratio m, the components of $\mathbf{D}^{(incl)}$ are equal to the values in the far field, except for D_{13}^{incl} and D_{23}^{incl} that are divided by m

$$
\begin{aligned}
&D_{11}^{incl} = D_{11}^{\infty},\ D_{22}^{incl} = D_{22}^{\infty},\ D_{33}^{incl} = -D_{11}^{incl} - D_{22}^{incl},\ D_{12}^{incl} = D_{12}^{\infty} \\
&D_{13}^{incl} = D_{13}^{\infty}/m,\ D_{23}^{incl} = D_{23}^{\infty}/m
\end{aligned}
\tag{46}
$$

For $m \to 0$, both D_{13}^{incl} and D_{23}^{incl} become unbounded. The products of the length a_3 and both D_{13}^{incl} and D_{23}^{incl} remain bounded

$$
\begin{aligned}
\lim_{a_3\to 0}\lim_{m\to 0} a_3 D_{13}^{incl} &= \lim_{a_3\to 0}\lim_{m\to 0} \frac{a_3 D_{13}^{\infty}}{1+2(m-1)S_{1313}} = a_2 D_{13}^{\infty}\left[E(k) + \frac{1}{r^2-1}\{F(k)-E(k)\}\right]^{-1} \\
\lim_{a_3\to 0}\lim_{m\to 0} a_3 D_{23}^{incl} &= \lim_{a_3\to 0}\lim_{m\to 0} \frac{a_3 D_{23}^{\infty}}{1+2(m-1)S_{2323}} = a_2 D_{23}^{\infty}\left[2E(k) + \frac{1}{r^2-1}\{E(k)-F(k)\}\right]^{-1}
\end{aligned}
\tag{47}
$$

where

$$
\begin{aligned}
&E(\theta,k) = \int_0^{\theta} \frac{\mathrm{d}\theta'}{\sqrt{1-k^2\sin\theta'}}, \quad F(\theta,k) = \int_0^{\theta} \sqrt{1-k^2\sin\theta'}\,\mathrm{d}\theta' \\
&\theta = \sin^{-1}\left(1-a_3^2/a_1^2\right)^{1/2}, \quad k = \left[(a_1^2-a_2^2)/(a_1^2-a_3^2)\right]^{1/2}
\end{aligned}
\tag{40}
$$

The inclusion vorticity tensor $\boldsymbol{W}^{(incl)}$ is

$$
W_{ij}^{incl} = W_{ij}^{\infty} + 2(1-m)\Pi_{ijkl} D_{kl}^{incl} \tag{41}
$$

where Π is defined as

$$
\Pi_{ijij} = (I_j - I_i)/8\pi \tag{42}
$$

In the limit of an elliptical inclusion (flat ellipsoid), i.e. $a_3 \to 0$, we obtain

where E and F denote the complete elliptic integrals of the first and second kind, respectively

$$
\begin{aligned}
&E(k) = \int_0^{\pi/2} \frac{\mathrm{d}\theta'}{\sqrt{1-k^2\sin\theta'}}, \quad F(k) = \int_0^{\pi/2} \sqrt{1-k^2\sin\theta'}\,\mathrm{d}\theta' \\
&k = \left[(a_1^2-a_2^2)/(a_1^2)\right]^{1/2} = \left(1-r^{-2}\right)^{1/2}
\end{aligned}
\tag{48}
$$

By interchanging a_1 and a_2 in the second equation in Eq. (47), we cover the $a_1 < a_2$ case

$$
\begin{aligned}
&\lim_{a_3\to 0}\lim_{m\to 0} a_3 D_{13}^{incl} = a_1 D_{13}^{\infty}\left[2E(k') + \frac{r^2}{r^2-1}\{F(k')-E(k')\}\right]^{-1} \\
&k' = \left(1-r^2\right)^{1/2}
\end{aligned}
\tag{49}
$$

Using Eq. (41) we find the components of the vorticity tensor for $a_3 \to 0$

$$\begin{aligned} W_{12}^{incl} &= W_{12}^{\infty} \\ W_{13}^{incl} &= W_{13}^{\infty} - D_{13}^{\infty} + D_{13}^{\infty}/m \\ W_{23}^{incl} &= W_{23}^{\infty} - D_{23}^{\infty} + D_{23}^{\infty}/m \end{aligned} \tag{50}$$

Hence, the components W_{13}^{incl} and W_{23}^{incl} are not bounded in the limit of $m \to 0$. The inclusion velocity gradient tensor $\mathbf{L}^{(incl)}$ for $a_3 \to 0$ yields

$$\begin{aligned} \mathbf{L}^{(incl)} &= \mathbf{D}^{(incl)} + \mathbf{W}^{(incl)} \\ &= \begin{pmatrix} D_{11}^{\infty} & D_{12}^{\infty} + W_{12}^{\infty} & W_{13}^{\infty} - D_{13}^{\infty} + 2D_{13}^{\infty}/m \\ D_{12}^{\infty} - W_{12}^{\infty} & D_{22}^{\infty} & W_{23}^{\infty} - D_{23}^{\infty} + 2D_{23}^{\infty}/m \\ D_{13}^{\infty} - W_{13}^{\infty} & D_{23}^{\infty} - W_{23}^{\infty} & D_{33}^{\infty} \end{pmatrix} \end{aligned} \tag{51}$$

The components L_{13}^{incl} and L_{23}^{incl} are unbounded for $m \to 0$. The remaining components of $\mathbf{L}^{(incl)}$ are equal to the values in the far field.

The velocity field inside the inclusion is obtained as a product of the velocity gradient and the position vector, i.e. $\overrightarrow{v^{incl}} = \mathbf{L}^{(incl)}\overrightarrow{x}$. For a flat ellipsoid, the third component of the position vector $x_3(=z')$ is infinitesimal and it is given as $x_3 = \pm a_3\sqrt{1-(x_1/a_1)^2-(x_2/a_2)^2}$ at the surfaces of the inclusion. The products of the components L_{13}^{incl} and L_{23}^{incl} and a_3 are finite and determine the discontinuity of the velocity field across the inclusion

$$\lim_{a_3\to 0}\lim_{m\to 0} a_3 L_{i3}^{incl} = 2\lim_{a_3\to 0}\lim_{m\to 0} a_3 D_{i3}^{incl}, \quad i = 1,2 \tag{52}$$

where the limits in the right hand side are already evaluated in Eq. (47).

Appendix B. Implementation

Both the internal and external solutions were implemented using MATLAB. The code was optimized for fast performance and a massive evaluation of the velocity vectors in the matrix. The trajectories of markers in the host are obtained by employing an in-built MATLAB adaptive ordinary differential equation solver and constantly reevaluating the external velocity solution according to the current orientation of the crack. The marker planes are discretized using an unstructured triangular mesh refined in the vicinity of the slip plane. The mesh is generated using the Triangle mesh generator (Shewchuk, 2002). The results are visualized using MATLAB and Paraview.

References

Abramowitz, M., Stegun, I.A., 1968. Handbook of Mathematical Functions with Formulas, Graphs, and Mathematical Tables. Dover, New York.

Alsop, G.I., Holdsworth, R.E., 2004. The geometry and topology of natural sheath folds: a new tool for structural analysis. Journal of Structural Geology 26, 1561–1589.

Cobbold, P.R., Quinquis, H., 1980. Development of sheath folds in shear regimes. Journal of Structural Geology 2, 119–126.

Eshelby, J.D., 1957. The determination of the elastic field of an ellipsoidal inclusion, and related problems. Proceedings of the Royal Society of London, Series A – Mathematical and Physical Sciences 241, 376–396.

Eshelby, J.D., 1959. The elastic field outside an ellipsoidal inclusion. Proceedings of the Royal Society of London, Series A – Mathematical and Physical Sciences 252 (1271), 561–569.

Exner, U., Mancktelow, N.S., Grasemann, B., 2004. Progressive development of s-type flanking folds in simple shear. Journal of Structural Geology 26, 2191–2201.

Freeman, B., 1987. The behavior of deformable ellipsoidal particles in threedimensional slow flows: implications for geological strain analysis. Tectonophysics 132, 297–309.

Fletcher, R.C., 2009. Deformable, rigid, and inviscid elliptical inclusions in a homogeneous incompressible anisotropic viscous fluid. Journal of Structural Geology 31, 382–387.

Grasemann, B., Stüwe, K., Vannay, J.C., 2003. Sense and non-sense of shear in flanking structures. Journal of Structural Geology 25, 19–34.

Grasemann, B., Martel, S., Passchier, C.W., 2005. Reverse and normal drag along a fault. Journal of Structural Geology 27, 999–1010.

Goldstein, H., Safko, J.L., Poole, C.P., 2002. Classical Mechanics. Addison-Wesley, San Francisco.

Gomez-Rivas, E., Bons, P.D., Griera, A., Carreras, J., Druguet, E., Evans, L., 2007. Strain and vorticity analysis using small-scale faults and associated drag folds. Journal of Structural Geology 29, 1882–1899.

Iacopini, D., Passchier, C.W., Koehn, D., Carosi, R., 2007. Fabric attractors in general triclinic flow systems and their application to high strain shear zones: a dynamical system approach. Journal of Structural Geology 29, 298–317.

Iglseder, C., Grasemann, B., Schneider, D.A., Petrakakis, K., Miller, C., Klötzli, U.S., Thöni, M., Zamolyi, A., Rambousek, C., 2009. I and S-type plutonism on Serifos (W-Cyclades, Greece). Tectonophysics 473, 69–83.

Jiang, D., Williams, P.F., 1998. High-strain zones: a unified model. Journal of Structural Geology 20, 1105–1120.

Kassir, M.K., Sih, G.C., 1975. Three-dimensional Crack Problems. Noordhoof, Leiden.

Kocher, T., Mancktelow, N.S., 2005. Dynamic reverse modelling of flanking structures: a source of quantitative kinematic information. Journal of Structural Geology 27, 1346–1354.

Kocher, T., Mancktelow, N.S., 2006. Flanking structure development in anisotropic viscous rock. Journal of Structural Geology 28, 1139–1145.

Lin, S., Jiang, D., 2001. Using along-strike variation in strain and kinematics to define the movement direction of curved transpressional shear zones: an example from northwestern Superior Province, Manitoba. Geology 29, 767–770.

Mandal, N., Mitra, A.K., Sarkar, S., Chakraborty, C., 2009. Numerical estimation of the initial hinge-line irregularity required for the development of sheath folds: a pure shear model. Journal of Structural Geology 31, 1161–1173.

Marques, F.O., Cobbold, P.R., 1995. Development of highly non-cylindrical folds around rigid ellipsoidal inclusions in bulk simple shear regimes: natural examples and experimental modelling. Journal of Structural Geology 17, 589–602.

Means, W.D., 1989. Stretching faults. Geology 17, 893–896.

Mulchrone, K.F., 2007. Modelling flanking structures using deformable high axial ratio ellipses: Insights into finite geometries. Journal of Structural Geology 29, 1216–1228.

Mura, T., 1987. Micromechanics of Defects in Solids. Kluwer Academic Publ., Dordrecht.

Passchier, C.W., 1997. The fabric attractor. Journal of Structural Geology 19, 113–127.

Passchier, C.W., 2001. Flanking structures. Journal of Structural Geology 23, 951–962.

Rosas, F., Marques, F.O., Luz, A., Coelho, S., 2002. Sheath folds formed by drag induced by rotation of rigid inclusions in viscous simple shear flow: nature and experiment. Journal of Structural Geology 24, 45–55.

Shewchuk, J.R., 2002. Delaunay refinement algorithms for triangular mesh generation. Computational Geometry: Theory and Applications 22, 21–74.

Sullivan, W.A., Law, R.D., 2007. Deformation path partitioning within the transpressional White Mountain shear zone, California and Nevada. Journal of Structural Geology 29, 583–598.

Wiesmayr, G., Grasemann, B., 2005. Sense and non-sense of shear in flanking structures with layer-parallel shortening: implications for fault-related folding. Journal of Structural Geology 27, 249–264.